


## AUTHOR QUERY FORM

	<p>Journal: J. Chem. Phys.</p>  <p>Article Number: JCP24-AR-04478</p>	<p>Please provide your responses and any corrections by annotating this PDF and uploading it to AIP's eProof website as detailed in the Welcome email.</p>
---	---	--

Dear Author,

Below are the queries associated with your article. Please answer all of these queries before sending the proof back to AIP.

**Article checklist:** In order to ensure greater accuracy, please check the following and make all necessary corrections before returning your proof.

1. **Is the title of your article accurate and spelled correctly?**
2. **Please check affiliations including spelling, completeness, and correct linking to authors.**
3. **Did you remember to include acknowledgment of funding, if required, and is it accurate?**

Location in article	Query/Remark: click on the Q link to navigate to the appropriate spot in the proof. There, insert your comments as a PDF annotation.
<a href="#">Q1</a>	Please check that the author names are in the proper order and spelled correctly. Also, please ensure that each author's given and surnames have been correctly identified (given names are highlighted in red and surnames appear in blue).
<a href="#">Q2</a>	Please check the definition of CCSD(T) and CASSCF.
<a href="#">Q3</a>	Please define MCPE at first occurrence.
<a href="#">Q4</a>	In the sentence beginning "As discussed in . . .," please confirm that "previous section" refers to Sec. III B.
<a href="#">Q5</a>	In the sentence beginning "In Subsection III E. . .," please confirm that "following subsection" refers to Subsection III E.
<a href="#">Q6</a>	We have reworded the sentence beginning "The second dehydrogenation step ..." for clarity. Please check that your meaning is preserved.
<a href="#">Q7</a>	In the sentence beginning "The reaction proceeds. . .," please confirm that "previous subsection" refers to Subsection III D.
<a href="#">Q8</a>	In the sentence beginning "As discussed in Secs. III A–III E . . .," please confirm that "previous subsections" refers to Secs. III A–III E.
<a href="#">Q9</a>	Please confirm the change in author's initials in Ref. 15.
<a href="#">Q10</a>	Please confirm the content in Refs. 26, 43, and 46, as we have inserted the required information.

*Continued on next page*

Continued from previous page

Q11	Please provide complete information in Ref. 29.
Q12	Please confirm ORCID IDs are accurate. If you wish to add an ORCID for any author that does not have one, you may do so now. For more information on ORCID, see <a href="https://orcid.org/">https://orcid.org/</a> .  Sapajan Ibragimov – 0000-0002-6015-7726 Andrey Lyalin – 0000-0001-6589-0006 Sonu Kumar – 0000-0002-3807-836X Yuriko Ono – Tetsuya Taketsugu – 0000-0002-1337-6694 Maciej Bobrowski – 0000-0002-9919-2430
Q13	Please check and confirm the Funder(s) and Grant Reference Number(s) provided with your submission: Ministry of Education, Culture, Sports, Science and Technology, Award/Contract Number JPMXP1122712807 Narodowa Agencja Wymiany Akademickiej, Award/Contract Number STE(E)R-ING Research Center for Computational Science, Okazaki, Japan, Award/Contract Number 23-IMS-C016 Please add any additional funding sources not stated above.

Thank you for your assistance.

Author Proof

# Theoretical design of nanocatalysts based on $(\text{Fe}_2\text{O}_3)_n$ clusters for hydrogen production from ammonia

Cite as: J. Chem. Phys. 162, 000000 (2025); doi: 10.1063/5.0242310

Submitted: 3 October 2024 • Accepted: 13 January 2025 •

Published Online: 9 99 9999



Sapajan Ibragimov,<sup>1,2</sup> Andrey Lyalin,<sup>3,4,a)</sup> Sonu Kumar,<sup>5</sup> Yuriko Ono,<sup>5</sup> Tetsuya Taketsugu,<sup>3,5</sup>   
and Maciej Bobrowski<sup>2</sup>

## AFFILIATIONS

<sup>1</sup> Faculty of Chemistry, Gdańsk University of Technology, Narutowi za 11/12, 80-233 Gdańsk, Poland

<sup>2</sup> Faculty of Technical Physics and Applied Mathematics, Gdańsk University of Technology, Narutowicza 11/12, 80-233 Gdańsk, Poland

<sup>3</sup> Department of Chemistry, Faculty of Science, Hokkaido University, Sapporo 060-0810, Japan

<sup>4</sup> Research Center for Energy and Environmental Materials (GREEN), National Institute for Materials Science, Namiki 1-1, Tsukuba 305-0044, Japan

<sup>5</sup> Institute for Chemical Reaction Design and Discovery (WPI-ICReDD), Hokkaido University, Sapporo 001-0021, Japan

<sup>a)</sup> Author to whom correspondence should be addressed: [lyalin@icredd.hokudai.ac.jp](mailto:lyalin@icredd.hokudai.ac.jp)

## ABSTRACT

The catalytic activities of high-spin small Fe(III) oxides have been investigated for efficient hydrogen production through ammonia decomposition, using the artificial force induced reaction method within the framework of density functional theory with the B3LYP hybrid exchange–correlation functional. Our results reveal that the adsorption free energy of  $\text{NH}_3$  on  $(\text{Fe}_2\text{O}_3)_n$  ( $n = 1-4$ ) decreases with increasing cluster size up to  $n = 3$ , followed by a slight increase at  $n = 4$ . The strongest  $\text{NH}_3$  adsorption energy, 28.55 kcal/mol, was found for  $\text{Fe}_2\text{O}_3$ , where  $\text{NH}_3$  interacts with a two-coordinated Fe site, forming an Fe–N bond with a length of 2.11 Å. A comparative analysis of  $\text{NH}_3$  dehydrogenation and  $\text{H}_2$  formation on various Fe(III) oxide sizes identifies the rate-determining steps for each reaction. We found that the rate-determining step for the full  $\text{NH}_3$  dehydrogenation on  $(\text{Fe}_2\text{O}_3)_n$  ( $n = 1-4$ ) is size-dependent, with the  $\text{NH}^* \rightarrow \text{N}^* + \text{H}^*$  reaction acting as the limiting step for  $n = 1-3$ . In addition, our findings indicate that  $\text{H}_2$  formation is favored following the partial decomposition of  $\text{NH}_3$  on Fe(III) oxides.

Published under an exclusive license by AIP Publishing. <https://doi.org/10.1063/5.0242310>

## I. INTRODUCTION

The ammonia decomposition reaction has recently received extensive attention due to its potential use as an alternative green energy source.<sup>1-5</sup> This reaction typically requires a catalyst and consists of two major steps. The first is ammonia dehydrogenation on the catalytic surface, leading to the formation of adsorbed nitrogen and hydrogen species. This is followed by nitrogen coupling, resulting in the formation of molecular nitrogen.<sup>6</sup> One of the key advantages of ammonia as a green energy source is its ability to be liquefied at low pressures and a relatively low temperature of 20 °C, making it an attractive candidate for hydrogen storage

and transportation. As with many other chemical processes, catalysts play a crucial role in ammonia decomposition to achieve fast and efficient  $\text{H}_2$  production. Experimental and theoretical studies have demonstrated that Ru-based catalysts are the most active for ammonia decomposition.<sup>6-8</sup> However, ruthenium's high cost and limited availability pose challenges for its large-scale industrial application. Therefore, developing new types of cost-effective catalysts for  $\text{NH}_3$  decomposition, based on non-noble metals or metal oxides, has become a significant area of research for effective hydrogen generation.<sup>9</sup> Numerous studies have focused on the activity of catalysts involving various metals and alloys.<sup>10</sup> Among the most studied non-noble metals, iron (Fe) stands out as a leading catalyst

due to its low cost and availability. While the reactivity of Fe is lower compared to other transition metals, it can be enhanced by using nanoparticles instead of extended surfaces. Indeed, it is well known that the reactivity of small-size clusters can be finely tuned by adjusting their size, geometry, and electronic structure, making them promising catalysts in various catalytic processes.<sup>11–15</sup> For example, Nishimaki *et al.*<sup>16</sup> experimentally studied ammonia decomposition on Fe nanoparticles of various grain sizes (20 nm–1  $\mu\text{m}$ ) in an ammonia steam environment. Their findings indicated that the highly reactive surface of nanoparticles enhances  $\text{NH}_3$  dissociation without increasing the nitrogen content in the gas phase, resulting in nitride phases that depend on the grain size and morphology.

As an alternative approach, ammonia decomposition reactions on small nanosized Fe clusters are frequently investigated using density functional theory (DFT) methods. Theoretical studies suggest that the mechanisms of ammonia decomposition involve stepwise dehydrogenation, where the rate-limiting step can vary depending on the size, type, and shape of the catalysts. Thus, Lanzani and Laasonen employed spin-polarized DFT to examine the adsorption and dissociation of  $\text{NH}_3$  on a single nanosized icosahedral  $\text{Fe}_{55}$  cluster.<sup>17</sup> Their research indicated that the overall reaction barrier for stepwise dehydrogenation was 1.48 eV, with different active sites on the  $\text{Fe}_{55}$  cluster (facets and vertices), where the rate-limiting step was the initial hydrogen dissociation. Similarly, Otero *et al.*<sup>18</sup> conducted a comprehensive comparative study on various sizes of Fe clusters ( $\text{Fe}_{16}$ ,  $\text{Fe}_{22}$ ,  $\text{Fe}_{32}$ ,  $\text{Fe}_{59}$ ,  $\text{Fe}_{80}$ ,  $\text{Fe}_{113}$ , and  $\text{Fe}_{190}$ ) and Fe(111) surfaces with additional adatoms. Their findings indicated that the reaction kinetics were influenced more by the strength of  $\text{NH}_3$  adsorption rather than the activation energy barrier. Stronger  $\text{NH}_3$  adsorption led to enhanced dissociation compared to desorption. The studies mentioned above primarily focus on the catalytic activities of large Fe clusters and Fe surfaces in the ammonia decomposition reaction. However, Zhang *et al.*<sup>19</sup> specifically investigated the activities of relatively small Fe clusters, ranging from single Fe atoms to  $\text{Fe}_4$  clusters. They found that the highest catalytic activity for stepwise  $\text{NH}_3$  dehydrogenation was observed with nonatomic iron clusters. Interestingly, they observed that the rate-limiting steps differed: co-adsorbate  $\text{NH}$  dissociation for Fe and  $\text{Fe}_3$  and co-adsorbate  $\text{NH}_2$  dissociation for  $\text{Fe}_2$  and  $\text{Fe}_4$ .

The  $\text{NH}_3$  decomposition reaction can be enhanced in the presence of oxygen, where it can proceed through various pathways, including ammonia oxidation and hydrogen evolution reactions. Moreover, metal oxides are commonly employed as catalyst supports in ammonia decomposition to enhance dispersion and catalytic stability. Among these supports, widely used materials include  $\text{Al}_2\text{O}_3$ ,  $\text{TiO}_2$ , as well as carbon nanotubes and nanofibers.<sup>7,20–24</sup> However, metal oxides not only serve as supports but also play a crucial role in hydrogen evolution reactions in electrocatalysis, where the oxidation state of metals significantly influences the catalytic activity of ammonia decomposition. In particular, iron-based oxides, such as  $\text{Fe}_2\text{O}_3$ , are extensively studied forms of iron oxide due to their low cost and abundance, although their activity and stability can vary depending on their structure and size.<sup>25–31</sup>

In this work, we elucidate the role of the size and structural effects on the catalytic activity of iron-oxide-based nano-catalysts

toward the efficient ammonia dehydrogenation process, which is the first step in the full ammonia decomposition reaction. In particular, we investigated the theoretical mechanisms of stepwise ammonia dehydrogenation on  $(\text{Fe}_2\text{O}_3)_n$  clusters with  $n = 1–4$  to compare the reactivity of different-sized Fe(III) oxides using the Artificial Force Induced Reaction (AFIR) method.<sup>32,33</sup> In addition, we examined the  $\text{NH}_3$  adsorption and various energy barriers for  $\text{NH}_3$  dehydrogenation on different active sites of Fe(III) oxides. Our investigation aims to contribute to the design of nanocatalysts based on  $\text{Fe}_2\text{O}_3$  by exploring the activity of small-sized Fe(III) oxide clusters.

## II. COMPUTATIONAL DETAILS

All calculations were performed using spin-unrestricted Kohn–Sham DFT with Becke’s three-parameter hybrid functional combined with the Lee, Yang, and Parr correlation functional, denoted as B3LYP.<sup>34–36</sup> In our calculations, we have employed the LANL2DZ<sup>37–39</sup> basis set with effective core potentials (ECPs), as well as the Pople-style 6-31+G\* basis set, equivalent to 6-31+G(d), which includes polarization (d) and diffuse (sp) functions, as it is implemented in the Gaussian 16 program.<sup>40</sup> These methods have been successfully applied to metals and metal oxide systems in previous studies. Thus, Glukhovtsev *et al.*<sup>41</sup> reported that the performance of the B3LYP/ECP method for systems containing iron with various types of bonding showed good agreement with the experimental data and high-level theoretical methods {coupled-cluster single double triple [CCSD(T)], MCPE, and complete active space self-consistent field (CASSCF)}. Similarly, Taguchi *et al.*<sup>42</sup> studied  $\text{Fe}_6\text{O}_2(\text{NO}_3)_4(\text{hmp})_8(\text{H}_2\text{O})_{22}$ ,  $[\text{Fe}_4(\text{N}_3)_6(\text{hmp})_6]$ , and  $\text{Fe}_8\text{O}_3(\text{OMe})(\text{pdm})_4(\text{pdmH})_4(\text{MeOH})_{25}$  clusters using the B3LYP/LANL2DZ level of theory, obtaining results that were consistent with the experimental data.

At the initial stage, the most stable isomers of iron trioxide for each selected size were investigated using the DFT method. A single iron trioxide molecule contains two  $\text{Fe}^{3+}$  ions; therefore, there are often several energetically accessible spin states (0, 1, 2, 3, 4, 5). For the starting cluster  $\text{Fe}_2\text{O}_3$ , the lowest energy structure corresponds to the nonet state with a total spin  $S = 4$ . For  $(\text{Fe}_2\text{O}_3)_2$ , the lowest energy solution was found with a total spin  $S = 10$ , indicating an increase in the number of  $\text{Fe}^{3+}$  ions, which raises the total spin projection. For  $(\text{Fe}_2\text{O}_3)_3$ , the lowest energy structure was found with a total spin  $S = 15$ , and finally, in the case of  $(\text{Fe}_2\text{O}_3)_4$ , the lowest energy structure had a total spin  $S = 20$ . Therefore, all clusters considered in our study were in a ferromagnetic configuration. We confirmed that spin contamination in the low-lying energy structures was negligible and conducted wavefunction stability analysis for all configurations to ensure the absence of instability.

To analyze the most favorable pathways of  $\text{NH}_3$  dehydrogenation and  $\text{H}_2$  formation reactions catalyzed by small  $(\text{Fe}_2\text{O}_3)_n$  ( $n = 1–4$ ) clusters, we applied the SC-AFIR and DS-AFIR methods implemented in the Global Reaction Route Mapping (GRRM) strategy.<sup>32,43–46</sup> These automated reaction path search methods have been successfully applied to many catalytic reactions in combination with DFT methods.<sup>33,47–50</sup> The basic idea in the AFIR strategy is to push fragments (reactants) A and B of the whole system together or pull them apart by minimizing the following AFIR function:<sup>32</sup>

$$F(Q) = E(Q) + \alpha \frac{\sum_{i \in A} \sum_{j \in B} \omega_{ij} r_{ij}}{\sum_{i \in A} \sum_{j \in B} \omega_{ij}} \quad (1)$$

The external force term in (1) perturbs the given adiabatic Potential Energy Surface (PES),  $E(Q)$ , with geometrical parameters  $Q$  in the AFIR function. Here,  $\alpha$  defines the strength of the artificial force, which depends on the weighted sum of the interatomic distances  $r_{ij}$  between atoms  $i$  and  $j$ , with the weights  $\omega_{ij}$  defined as

$$\omega_{ij} = \left[ \frac{R_i + R_j}{r_{ij}} \right]^6, \quad (2)$$

where  $R_i$  and  $R_j$  are the covalent radii of atoms  $i$  and  $j$ , respectively. The force parameter  $\alpha$  in (1) can be expressed as follows:

$$\alpha = \frac{\gamma}{\left[ 2^{-1/6} - (1 + \sqrt{1 + \gamma/\varepsilon})^{-1/6} \right] R_0}, \quad (3)$$

where  $R_0$  and  $\varepsilon$  are the parameters corresponding to interatomic Lennard-Jones potentials and the parameter  $\gamma$  has a physical meaning of a collision energy.

This perturbation of the PES facilitates the exploration of additional approximate transition states (TS) and local minima on the surface. The model collision energy parameter  $\gamma$  in (3) serves as an approximate upper limit for the barrier height that the system can be affected by the AFIR function.<sup>32</sup> In our calculations,  $\gamma$  was set to 300 kJ/mol for the entire system. During the initial reaction path search, the LANL2DZ basis set was applied with an artificial force to yield approximate products and transition states (TS). Subsequently, we utilized the 6-31+G\* basis set to optimize these approximate transition states and local minima without the artificial force, employing the Locally Updated Plane (LUP) method. The vibrational frequency calculations have been performed to confirm the nature of the stationary points, whether they are minima or transition states. The results presented in this paper include reaction route mapping at the B3LYP/LANL2DZ level and reaction pathways at the B3LYP/6-31+G(d) level.

The binding energy  $E_b$  per unit  $n$  of a  $(\text{Fe}_2\text{O}_3)_n$  cluster is defined as follows:

$$E_b = - \frac{E_{el}((\text{Fe}_2\text{O}_3)_n) + E_{ZPE}((\text{Fe}_2\text{O}_3)_n) - [2nE(\text{Fe}) + 3nE(\text{O})]}{n}, \quad (4)$$

where  $E_{el}((\text{Fe}_2\text{O}_3)_n)$  and  $E_{ZPE}((\text{Fe}_2\text{O}_3)_n)$  are the electronic and zero-point energies of a cluster  $(\text{Fe}_2\text{O}_3)_n$  with a number of units  $n$ , while  $E(\text{Fe})$  and  $E(\text{O})$  are the energies of free Fe and O atoms, respectively.

The standard free energy of adsorption,  $\Delta G_{ads}$ , is given as

$$\Delta G_{ads} = G(\text{NH}_3@(\text{Fe}_2\text{O}_3)_n) - (G((\text{Fe}_2\text{O}_3)_n) + G(\text{NH}_3)), \quad (5)$$

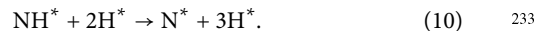
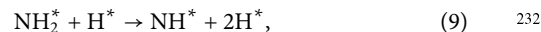
where  $G(\text{NH}_3@(\text{Fe}_2\text{O}_3)_n)$  is the free energy of the most stable structure of the  $(\text{Fe}_2\text{O}_3)_n$  cluster with the adsorbed ammonia molecule,  $G((\text{Fe}_2\text{O}_3)_n)$  is the free energy of the bare  $(\text{Fe}_2\text{O}_3)_n$  cluster, and  $G(\text{NH}_3)$  is the free energy of a single ammonia molecule. The values of free energy  $G$  in (5) can be calculated as follows:

$$G = E_{el} + E_{ZPE} - TS, \quad (6)$$

where  $E_{el}$  and  $E_{ZPE}$  are the electronic and zero-point energies of the system,  $S$  is the entropy of the system, and  $T$  is the temperature. The reported energies have been corrected for the basis set superposition error (BSSE).

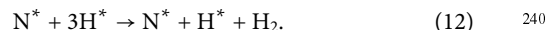
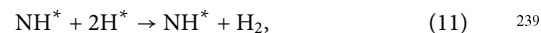
### III. RESULTS AND DISCUSSION

In the present work, we systematically investigated the ammonia decomposition reaction mechanisms on  $(\text{Fe}_2\text{O}_3)_n$  clusters of various sizes  $n$ , where  $n = 1-4$ . First, we identified approximate reaction pathways for the interactions between  $\text{NH}_3$  molecules and the most stable isomers of  $(\text{Fe}_2\text{O}_3)_n$  clusters using the AFIR technique. The obtained AFIR pathways were subsequently re-optimized along the minimum energy path using the Locally Updated Plane (LUP) method, without applying artificial forces. We calculated various reaction mechanisms and the stepwise dissociation<sup>51</sup> of hydrogen atoms from nitrogen-containing compounds on Fe(III) oxide clusters, following the elementary steps,



Here, \* denotes a free cluster, while the adsorbed intermediates on the surface of the  $(\text{Fe}_2\text{O}_3)_n$  cluster are represented by \* in the superscript.

Finally, the adsorbed hydrogen atoms on the  $(\text{Fe}_2\text{O}_3)_n$  clusters can combine to produce molecular hydrogen ( $\text{H}_2$ ),



This paper is organized as follows. We first discuss the structures of free clusters, followed by the adsorption of  $\text{NH}_3$  on the most stable isomers of  $(\text{Fe}_2\text{O}_3)_n$ ,  $n = 1-4$ , clusters. We then examine the complete dehydrogenation and  $\text{H}_2$  formation processes for each cluster size.

#### A. Structure of $(\text{Fe}_2\text{O}_3)_n$ clusters with $n = 1-4$

Figure 1 demonstrates the most stable structures of small  $(\text{Fe}_2\text{O}_3)_n$  clusters with  $n = 1-4$ , as obtained in the present work using the automated GRRM approach. A total of up to 60 isomer structures have been obtained for each cluster size  $n$ . The low-energy isomers for each cluster size, along with their relative binding energies, are presented in Figs. S2-S5. We found that the most stable structure of the smallest  $\text{Fe}_2\text{O}_3$  cluster is a nonet kite-like type with a binding energy  $E_b = 362.7$  kcal/mol. The kite-like structure is a commonly studied configuration<sup>52,53</sup> and was previously investigated by Sierka *et al.*,<sup>54</sup> who observed the most stable spin configuration for this structure to be  $S = 0$ . In contrast, we found that the lowest energy structure corresponds to a nonet state with  $S = 4$ , while the singlet kite-like structure is 0.62 kcal/mol less stable at the B3LYP/6-31+G\* level of theory as shown in Table S1. This finding is also compared with another hybrid functional, M06,<sup>55</sup> and a range-separated func-



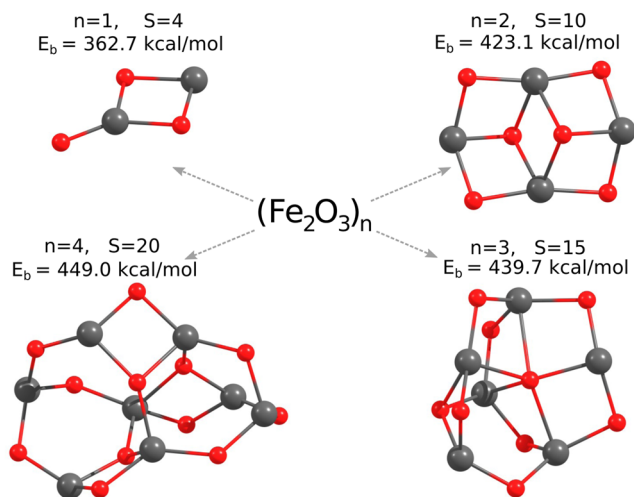


FIG. 1. Most stable structures of  $(\text{Fe}_2\text{O}_3)_n$  clusters with  $n = 1-4$ . The values of the total spin  $S$  and the binding energy  $E_b$  of the clusters are mentioned in the legends.

tional with additional dispersion correction, wB97XD,<sup>56</sup> in Table S1. The results of our calculations show that the absolute binding energy of  $(\text{Fe}_2\text{O}_3)_n$  rapidly increases with the increasing cluster size  $n$  from 1 to 2 by 60.4 kcal/mol. However, further growth in the binding energy with the cluster size slows down, demonstrating a tendency for saturation as  $n$  increases.

## B. Ammonia adsorption on $(\text{Fe}_2\text{O}_3)_n$ clusters

The adsorption of ammonia on  $(\text{Fe}_2\text{O}_3)_n$  clusters is a crucial initial step in the whole dehydrogenation process. Figure 2 demonstrates the most stable adsorption configurations of the  $\text{NH}_3$

molecule on  $(\text{Fe}_2\text{O}_3)_n$  clusters with  $n = 1-4$ . The corresponding basis set superposition error corrected free energies of adsorption and Fe-N bond distances are shown in Table I at 0 K. Our calculations show that the adsorption of  $\text{NH}_3$  on the smallest  $\text{Fe}_2\text{O}_3$  cluster is the most stable among all cluster sizes considered in this study, with an adsorption free energy of  $-28.55$  kcal/mol. This finding is corroborated by Mulliken charge analysis, which shows that more electrons are shared between the lone pair of the N atom and the 3d orbitals of  $\text{Fe}^{2+}$  for  $n = 1$ . Meanwhile, for larger cluster sizes with  $n = 2-4$ , which primarily contain  $\text{Fe}^{3+}$ , the electron density is more localized over the bonding region, as also reported by Sierka *et al.*<sup>54</sup> Therefore, bonding occurs with the nitrogen lone pair.

Our theoretical analysis indicates that the adsorption energy  $\Delta G_{ads}$  of ammonia on  $(\text{Fe}_2\text{O}_3)_n$  clusters decreases from  $n = 1$  to  $n = 3$ , followed by a slight increase for  $n = 4$ . A similar trend in the change of adsorption energy with the cluster size was reported by Zhou *et al.*<sup>57</sup> for  $\text{Ru}_n/\text{CNT}$  systems. We also compared the adsorption energy of  $\text{NH}_3$  on different metal and metal oxides in Table I. The obtained  $\text{NH}_3$  adsorption energies on  $(\text{Fe}_2\text{O}_3)_n$  clusters are about 8 kcal/mol higher than the data reported by Zhang *et al.* for the Ru(0001) surface.<sup>58</sup> Moreover, the adsorption of  $\text{NH}_3$  and  $\text{NO}_x$  on the  $\gamma\text{-Fe}_2\text{O}_3(111)$  surface was studied by Huang *et al.*<sup>59</sup> using periodic density functional calculations. They calculated adsorption energies on the octahedral and tetrahedral sites of  $\gamma\text{-Fe}_2\text{O}_3(111)$  to be  $-2.13$  and  $-21.68$  kcal/mol, respectively. Similarly, our calculated  $\text{NH}_3$  adsorption energies on  $(\text{Fe}_2\text{O}_3)_n$  clusters for  $n = 3$  and  $n = 4$  are close to the data reported by Huang *et al.*,<sup>59</sup> as the adsorption of  $\text{NH}_3$  on the three-coordinated  $\text{Fe}^{3+}$  site resembles the tetrahedral site of  $\gamma\text{-Fe}_2\text{O}_3(111)$ , while the adsorption on the four-coordinated  $\text{Fe}^{3+}$  site resembles the octahedral site of  $\gamma\text{-Fe}_2\text{O}_3$ .

As mentioned above, the calculated adsorption energies indicate that the adsorption of an  $\text{NH}_3$  molecule on  $(\text{Fe}_2\text{O}_3)_n$  clusters

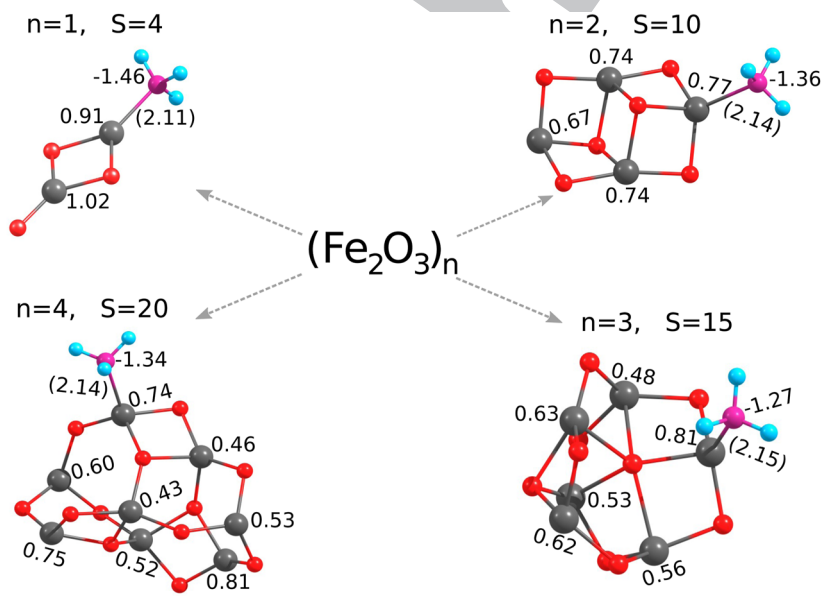


FIG. 2. Optimized geometries of  $\text{NH}_3$  adsorbed on  $(\text{Fe}_2\text{O}_3)_n$  clusters for  $n = 1-4$ . N-Fe distances (Å) are shown in parentheses, along with the partial atomic charges on neighboring atoms. The values of the total spin  $S$  of the clusters are mentioned in the legends.

313 **TABLE I.** NH<sub>3</sub> adsorption free energy  $\Delta G_{ads}$  and d(Fe–N) bond length in various  
314 sizes of (Fe<sub>2</sub>O<sub>3</sub>)<sub>n</sub>, where n = 1–4.  
315

	$\Delta G_{ads}$ (kcal/mol)	Fe–N (Å)	Reference
316 NH <sub>3</sub> /Fe <sub>2</sub> O <sub>3</sub>	–28.55	2.11	
317			
318 NH <sub>3</sub> /(Fe <sub>2</sub> O <sub>3</sub> ) <sub>2</sub>	–28.36	2.14	This work
319			
320 NH <sub>3</sub> /(Fe <sub>2</sub> O <sub>3</sub> ) <sub>3</sub>	–27.65	2.15	
321			
322 NH <sub>3</sub> /ZnFe <sub>2</sub> O <sub>4</sub> (110)	–48.54	Zn–N (2.03)	<sup>a</sup>
323	–41.52	Fe–N (1.99)	
324 NH <sub>3</sub> /Ru(0001)	–20.52	Ru–N (2.17)	<sup>b</sup>
325			
326 NH <sub>3</sub> /Fe <sub>2</sub> O <sub>3</sub> /AC	–49.12, –37.35	...	<sup>c</sup>
327	–26.29, –31.13	...	
328			
329 NH <sub>3</sub> /γ-Fe <sub>2</sub> O <sub>3</sub> nano	–37.52	...	<sup>d</sup>
330 NH <sub>3</sub> /γ-Fe <sub>2</sub> O <sub>3</sub> (111)	–21.68	Fe <sub>tet</sub> –N (2.13)	<sup>e</sup>
331	–2.13	Fe <sub>oct</sub> –N (2.101)	

332 <sup>a</sup>Reference 60.

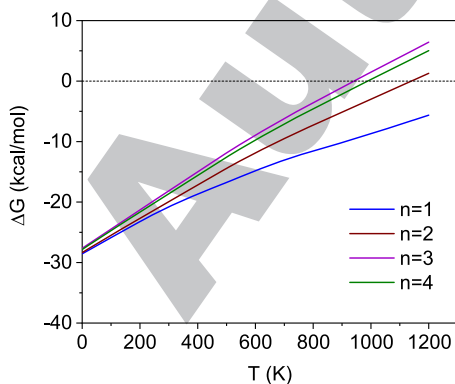
333 <sup>b</sup>Reference 58.

334 <sup>c</sup>Reference 61.

335 <sup>d</sup>Reference 62.

336 <sup>e</sup>Reference 59.

338 (n = 1–4) weakens as the cluster size increases from n = 1 to n = 3.  
339 In industrial processes, the dehydrogenation of ammonia typically  
340 occurs at high temperatures, often in the range of 400–700 °C,  
341 depending on the specific catalysts and conditions used. Therefore, it  
342 is important to determine the range of temperatures at which ammonia  
343 adsorption on (Fe<sub>2</sub>O<sub>3</sub>)<sub>n</sub> remains stable. Figure 3 demonstrates  
344 the temperature dependence of  $\Delta G_{ads}$  in the range from 0 to 1200 K  
345 for the most stable adsorption configurations of NH<sub>3</sub> on (Fe<sub>2</sub>O<sub>3</sub>)<sub>n</sub>  
346 clusters (n = 1–4). The negative values of  $\Delta G_{ads}$  correspond to stable  
347 adsorption. As shown in Fig. 3, NH<sub>3</sub> adsorbed on the smallest  
348 Fe<sub>2</sub>O<sub>3</sub> cluster is stable across the whole range of the considered



338 **FIG. 3.** Temperature dependence of the adsorption free energy for NH<sub>3</sub> adsorption  
339 on (Fe<sub>2</sub>O<sub>3</sub>)<sub>n</sub> clusters with n = 1–4 at 1 atm.

351 temperatures. However, for larger cluster sizes, ammonia adsorption  
352 becomes energetically unfavorable at temperatures of 1140 (K), 940  
353 (K), and 989 (K) for n = 2, 3, and 4, respectively.

### 354 C. NH<sub>3</sub> decomposition on Fe<sub>2</sub>O<sub>3</sub>

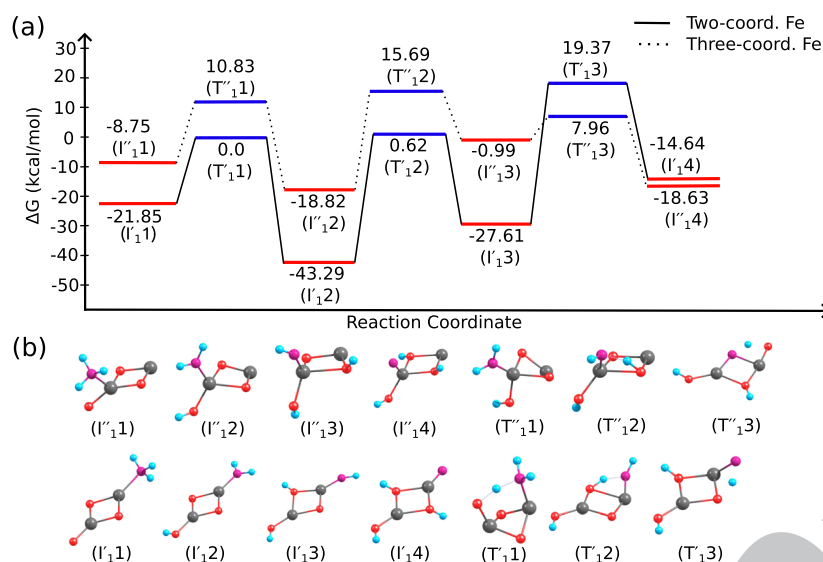
355 Here, we discuss the complete NH<sub>3</sub> decomposition and H<sub>2</sub> forma-  
356 tion reactions (7)–(12) on the smallest considered cluster, Fe<sub>2</sub>O<sub>3</sub>,  
357 at room temperature, T = 298.15 K, explored by the AFIR method.  
358 This method allows for the automatic exploration of the full reaction  
359 path network, systematically accounting for the variety of possi-  
360 ble isomer structures and adsorption sites. This is an important  
361 approach in nanocatalysis because it has been demonstrated that the  
362 most stable structures are not always the most reactive. Therefore, a  
363 systematic search for reaction pathways that accounts for the contri-  
364 butions of low-energy isomers is required to accurately describe the  
365 catalytic properties of clusters at finite temperatures.<sup>49</sup>

366 To illustrate the isomer and reaction-site effects, we explicitly  
367 consider two different isomers of the Fe<sub>2</sub>O<sub>3</sub> cluster: the most sta-  
368 ble kite-like structure with one terminal oxygen atom and the linear  
369 structure isomer with two terminal oxygen atoms, which is 6.24  
370 kcal/mol less stable (see Fig. S2). The kite-like structure possesses  
371 two types of catalytically active metal centers—two-coordinated and  
372 three-coordinated Fe sites. Therefore, we consider the adsorption  
373 and decomposition of an NH<sub>3</sub> molecule on both of them.

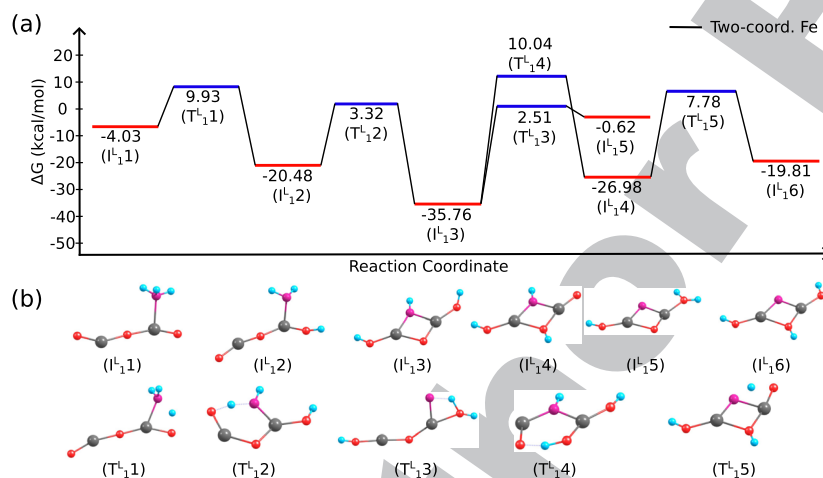
374 Figure 4(a) demonstrates that the adsorption of NH<sub>3</sub> on the  
375 kite-like Fe<sub>2</sub>O<sub>3</sub> cluster is an exothermic reaction, occurring at both  
376 the two-coordinated and three-coordinated Fe sites. The adsorption  
377 free energies are –21.85 kcal/mol for the two-coordinated Fe site  
378 (intermediate I<sub>1</sub><sup>1</sup>) and –8.75 kcal/mol for the three-coordinated Fe  
379 site (intermediate I<sub>1</sub><sup>1</sup>). The optimized structures of all intermediates  
380 (I) and transition states (T) along the reaction pathways are shown  
381 in Figs. 4(b) and 5(b), for the kite-like and linear clusters, respec-  
382 tively. Here, the lower index corresponds to the cluster size n, while  
383 the numbering corresponds to the order of intermediates (transition  
384 states) along the reaction path. As discussed in Sec. III B, the most  
385 stable adsorption site for NH<sub>3</sub> is the two-coordinated Fe site, with an  
386 Fe–N bond length of 2.11 Å. In contrast, the Fe–N bond length at the  
387 three-coordinated Fe site is 2.16 Å. These findings are supported by  
388 the fact that NH<sub>3</sub> adsorption highly depends on the local geometry  
389 and electronic structure of the catalyst.

390 In the case of the Fe<sub>2</sub>O<sub>3</sub> kite-like structure, the first dehy-  
391 drogenation reaction is the second step in the reaction mecha-  
392 nism, occurring after adsorption with the activation barriers of  
393 21.85 kcal/mol and 19.58 kcal/mol through the reaction paths  
394 I<sub>1</sub><sup>1</sup>–T<sub>1</sub><sup>1</sup>–I<sub>1</sub><sup>2</sup> and I<sub>1</sub><sup>1</sup>–T<sub>1</sub><sup>1</sup>–I<sub>1</sub><sup>2</sup>, respectively. The reactions on these  
395 two-coordinated and three-coordinated active sites are exothermic  
396 by 21.44 and 10.07 kcal/mol, respectively. However, the first dehy-  
397 drogenation of NH<sub>3</sub> on the linear-type structure [Fig. 5(a)] occurs  
398 with a smaller activation barrier of 13.96 kcal/mol via the reaction  
399 path I<sub>1</sub><sup>L</sup>–T<sub>1</sub><sup>L</sup>–I<sub>1</sub><sup>2</sup>, demonstrating that the less stable linear isomer is  
400 more reactive.

401 The role of the Fe<sub>2</sub>O<sub>3</sub> isomer structure on NH<sub>3</sub> adsorption and  
402 the first hydrogen atom transfer was previously studied by Xie *et al.*<sup>61</sup>  
403 They performed DFT-D3 calculations on the adsorption mecha-  
404 nisms of different molecules (NH<sub>3</sub>, NO, and O<sub>2</sub>) on activated car-  
405 bon (AC) supported iron-based catalysts Fe<sub>x</sub>O<sub>y</sub>/AC. The calculated  
406 adsorption electronic energies of NH<sub>3</sub> were –37.4 and –53.7



**FIG. 4.** (a) Energy profile for the  $\text{NH}_3^* \rightarrow \text{NH}_2^* + \text{H}^* \rightarrow \text{NH}^* + 2\text{H}^* \rightarrow \text{N}^* + 3\text{H}^*$  reaction path on the kite-like isomer of  $\text{Fe}_2\text{O}_3$  at  $T = 298.15$  K. (b) Geometries of the optimized equilibrium and transition states along the reaction path.

424  
425  
426  
427

**FIG. 5.** (a) Energy profile for the  $\text{NH}_3^* \rightarrow \text{NH}_2^* + \text{H}^* \rightarrow \text{NH}^* + 2\text{H}^* \rightarrow \text{N}^* + 3\text{H}^*$  reaction path on the linear-type isomer of  $\text{Fe}_2\text{O}_3$  at  $T = 298.15$  K. (b) Geometries of the optimized equilibrium and transition states along the reaction path.

428  
429  
430  
431  
432

kcal/mol on different isomers of  $\text{Fe}_2\text{O}_3/\text{AC}$ , and the first hydrogen atom transfer had an activation barrier of 15.5 kcal/mol. Similarly, the adsorption and dehydrogenation of ammonia on different metal oxides were investigated by Erdtman and co-workers<sup>63</sup> for the application of gas sensors. They reported that the adsorption energy of  $\text{NH}_3$  on the  $\text{RuO}_2(110)$  surface is  $-38.24$  kcal/mol, and the first N–H bond cleavage had an activation energy barrier of 17.45 kcal/mol.

The third step of the  $\text{NH}_3$  dehydrogenation reaction (9) involves the dissociation of the adsorbed  $\text{NH}_2^*$  intermediate into  $\text{NH}^*$  and  $\text{H}^*$  species. In this step, the abstracted hydrogen atom transfers to one of the oxygen atoms in the cluster. Figure 4(a) demonstrates that in the case of the kite-like structure, the energy barriers for this step are 43.91 and 34.51 kcal/mol, corresponding to the reaction paths  $\text{I}''_1\text{2} - \text{T}''_1\text{2} - \text{I}''_1\text{3}$  and  $\text{I}''_1\text{2} - \text{T}''_1\text{2} - \text{I}''_1\text{3}$ .

In the fourth step (10), the adsorbed  $\text{NH}^*$  intermediate further dissociates into  $\text{N}^*$  and  $\text{H}^*$  species as shown in Fig. 4(a). The reaction barriers associated with this step are 46.98 and 8.95 kcal/mol for

the two-coordinated and three-coordinated reaction paths, respectively. The decomposition of  $\text{NH}_3$  on kite-like structures becomes endothermic starting from the third step (9). Our calculations reveal that  $\text{NH}_3$  dehydrogenation has a high energy barrier when the  $\text{NH}_3$  molecule is adsorbed at a two-coordinated Fe site, which is the most stable adsorption site. Meanwhile, the dehydrogenation of the adsorbed  $\text{NH}_3$  at a three-coordinated Fe site has a considerably lower activation barrier of 8.95 kcal/mol for the reaction step (10).

Overall, for the  $\text{NH}_3$  decomposition reaction on the kite-like  $\text{Fe}_2\text{O}_3$  structure, with initial  $\text{NH}_3$  adsorption on the two-coordinated Fe atom, the rate-limiting step is the fourth reaction (10), with a barrier of 46.98 kcal/mol. Alternatively, for the less favorable  $\text{NH}_3$  adsorption on the three-coordinated Fe atom, the rate-limiting step is the third reaction step (9), with a barrier of 34.51 kcal/mol.

The reaction pathway calculated for  $\text{NH}_3$  decomposition on the linear-type  $\text{Fe}_2\text{O}_3$  isomer is shown in Fig. 5(a), and respective

433  
434  
435  
436  
437  
438  
439  
440  
441  
442  
443  
444  
445  
446  
447  
448  
449



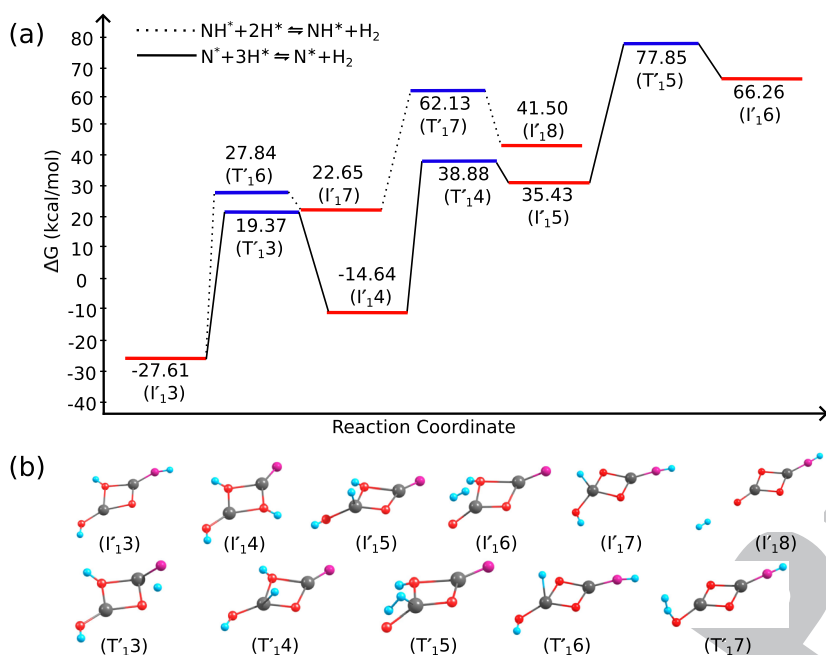


**FIG. 6.** (a) Energy profile for H<sub>2</sub> formation on the kite-like Fe<sub>2</sub>O<sub>3</sub> cluster at T = 298.15 K. (b) Geometries of the optimized equilibrium and transition states along the reaction path.

457  
458  
459

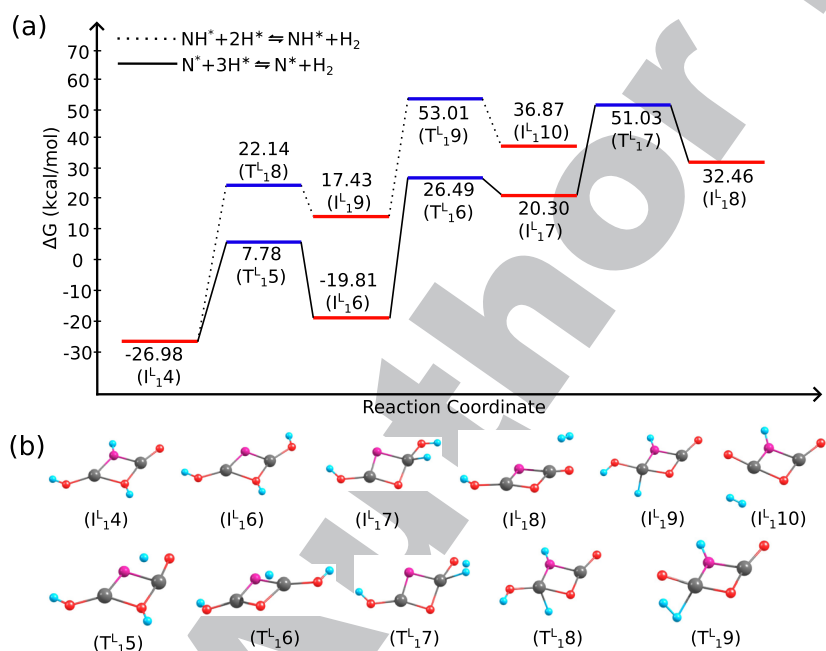


**FIG. 7.** (a) Energy profile for H<sub>2</sub> formation on the linear isomer of the Fe<sub>2</sub>O<sub>3</sub> cluster at T = 298.15 K. (b) Geometries of the optimized equilibrium and transition states along the reaction path.

460  
461  
462  
463

intermediate and transition state structures are shown in Fig. 5(b). Since this structure consists of two iron atoms connected through a central oxygen, each containing a terminal oxygen, the reaction mechanism differs slightly from that of the kite-like isomer. For instance, in the third step of the reaction, the second hydrogen from the adsorbed NH<sub>2</sub>\* intermediate is transferred to the second terminal oxygen. The energy barrier for this step on the linear-type

structure is 23.8 kcal/mol, as shown in the reaction path (I<sup>1</sup><sub>2</sub>–T<sup>1</sup><sub>2</sub>–I<sup>1</sup><sub>3</sub>) in Fig. 5(a).

The fourth step on this isomer is not straightforward, involving the central oxygen atom breaking its bond with one of the neighboring iron atoms while forming an Fe–N–Fe bridge. This process leads to two different intermediates: the formation of the adsorbed H<sub>2</sub>O\* and the transfer of a hydrogen atom from one side of the Fe–N–Fe

464  
465  
466  
467  
468  
469  
470

bridge to the other. Subsequently, the final dehydrogenation step from the  $\text{NH}^*$  intermediate occurs, with an activation energy barrier of 34.76 kcal/mol.

As a next step, we consider possible  $\text{H}_2$  formation via reactions (11) and (12) on the kite-like and linear isomers of the  $\text{Fe}_2\text{O}_3$  cluster. The possible pathways for  $\text{H}_2$  formation in the case of the most stable ammonia adsorption on the two-coordinated site ( $I'$  intermediates) of the kite-like  $\text{Fe}_2\text{O}_3$  isomer are shown in Fig. 6(a), while the corresponding structures of the optimized equilibrium and transition states along the reaction path are illustrated in Fig. 6(b).

Note that  $\text{H}_2$  formation can occur after the partial decomposition of ammonia in reaction (11), starting from the intermediate ( $I_1^3$ ) via the path  $I_1^3-T_1^6-I_1^7-T_1^7-I_1^8$ . Meanwhile,  $\text{H}_2$  formation can occur via the full decomposition of ammonia in reaction (12), through the intermediate ( $I_1^4$ ) via the path  $I_1^4-T_1^4-I_1^5-T_1^5-I_1^6$ . In both cases, the reaction pathways include breaking one O-H bond and forming an Fe-H bond. The  $\text{H}_2$  formation barriers through these intermediates are 89.74 and 92.49 kcal/mol, respectively. From these results, we conclude that  $\text{H}_2$  formation on the kite-like  $\text{Fe}_2\text{O}_3$  structure is more favorable via reaction (11), with the  $\text{NH}^*$  intermediate remaining adsorbed on the cluster. The  $\text{H}_2$  formation reaction, starting from ( $I_1^4$ ), is the rate-limiting step in molecular hydrogen formation on the kite  $\text{Fe}_2\text{O}_3$  cluster.

Similarly, the  $\text{H}_2$  formation reaction pathways on the linear-type structure of  $\text{Fe}_2\text{O}_3$  are shown in Fig. 7(a), while the

optimized equilibrium and transition states along the reaction path are illustrated in Fig. 7(b). The  $\text{H}_2$  formation through the  $\text{NH}^*$  intermediate ( $I_1^4$ ) via the reaction path  $I_1^4-T_1^8-I_1^9-T_1^9-I_1^{10}$  has an energy barrier of 79.99 kcal/mol. Meanwhile,  $\text{H}_2$  formation through the intermediate ( $I_1^6$ ) via the reaction path  $I_1^6-T_1^6-I_1^7-T_1^7-I_1^8$  has an activation energy of 70.84 kcal/mol, which is about 10 kcal/mol lower energy than the reaction path through the intermediate ( $I_1^4$ ).

Overall, our calculated reaction pathways for  $\text{H}_2$  formation show a similar pattern for both kite-type and linear-type  $\text{Fe}_2\text{O}_3$ , where  $\text{H}_2$  formation in reactions (11) and (12) take place via breaking one O-H bond and forming an intermediate Fe-H bond. However, from both thermodynamic and kinetic perspectives,  $\text{H}_2$  formation on the two types of  $\text{Fe}_2\text{O}_3$  structures varies. Reaction (11) is more favorable on the kite-like structure, while reaction (12) is more favorable on the linear structure. This highlights that the rate-limiting step for  $\text{H}_2$  formation is highly dependent on the catalyst's structure.

#### D. $\text{NH}_3$ decomposition on $\text{Fe}_4\text{O}_6$

In Subsection III E, we discuss the catalytic activity of  $(\text{Fe}_2\text{O}_3)_2$  toward  $\text{NH}_3$  dehydrogenation and  $\text{H}_2$  formation reactions. On the basis of adsorption characteristics discussed in Sec. III B, the three-fold coordinate  $\text{Fe}^{3+}$  site of the  $\text{Fe}_4\text{O}_6$  cluster is the most stable site for  $\text{NH}_3$  adsorption. A complete reaction pathway for the stepwise

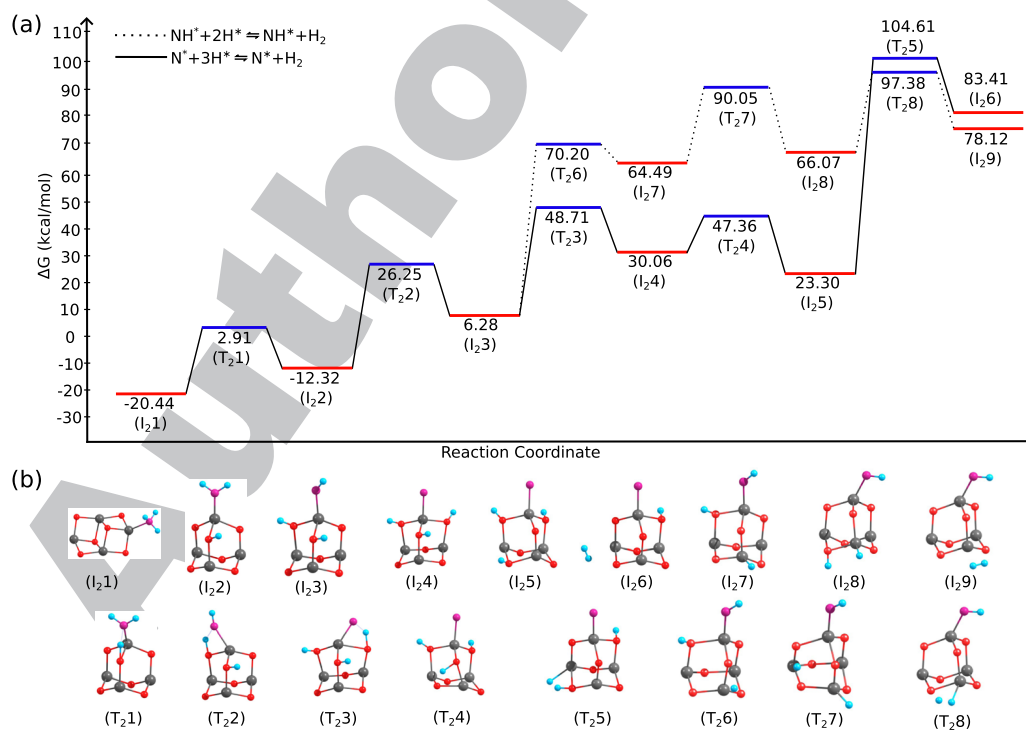


**FIG. 8.** (a) Energy profile for the  $\text{NH}_3 \rightarrow \text{NH}_2^* + \text{H}^* \rightarrow \text{NH}^* + 2\text{H}^* \rightarrow \text{N}^* + 3\text{H}^*$  and  $\text{H}_2$  formation reaction paths on the  $(\text{Fe}_2\text{O}_3)_2$  cluster at  $T = 298.15$  K. (b) Geometries of the optimized equilibrium and transition states along the reaction path.

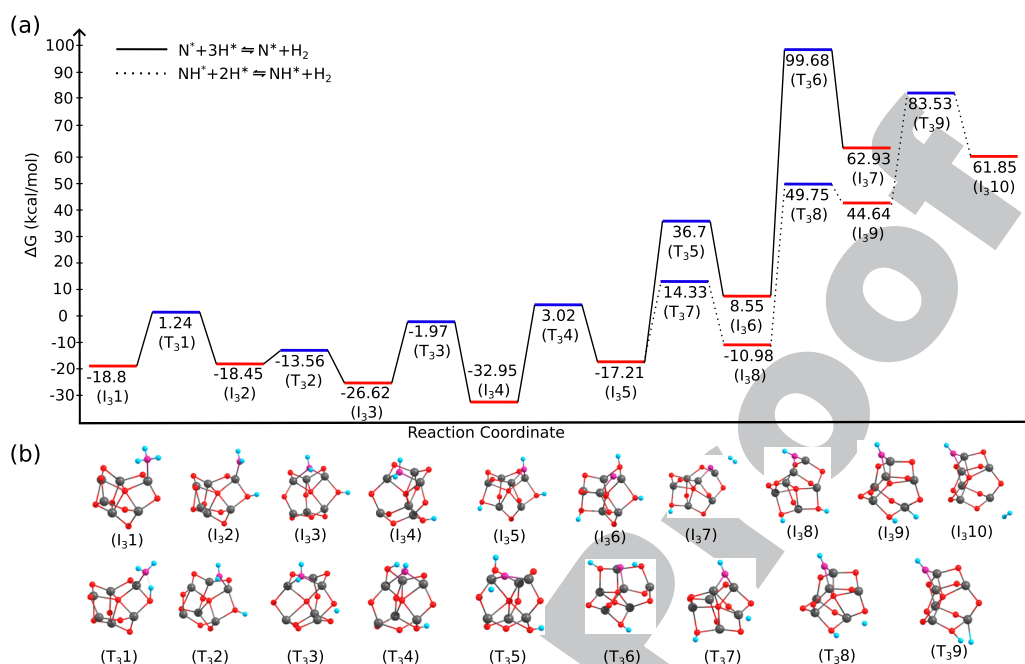


**FIG. 9.** (a) Energy profile for the  $\text{NH}_3^* \rightarrow \text{NH}_2^* + \text{H}^* \rightarrow \text{NH}^* + 2\text{H}^* \rightarrow \text{N}^* + 3\text{H}^*$  and  $\text{H}_2$  formation reaction paths on the  $(\text{Fe}_2\text{O}_3)_3$  cluster at  $T = 298.15$  K. (b) Geometries of the optimized equilibrium and transition states along the reaction path.

522  
523

524 decomposition of  $\text{NH}_3$  and the formation of  $\text{H}_2$  reactions on the  
525  $(\text{Fe}_2\text{O}_3)_2$  cluster is depicted in Fig. 8(a), and the corresponding  
526 intermediate and transition state structures are shown in Fig. 8(b).  
527 From this point forward, the first dehydrogenation step follows  
528 starting from the intermediate ( $\text{I}_21$ ), where the  $\text{NH}_3$  molecule inter-  
529 acts with the three-coordinated Fe site of the  $(\text{Fe}_2\text{O}_3)_2$  cluster by  
530 transferring a hydrogen to its one of neighboring oxygens via the  
531 reaction pathway ( $\text{I}_21$ – $\text{T}_21$ – $\text{I}_22$ ) and the reaction barrier of this  
532 step is 23.35 kcal/mol, which is 1.5 kcal/mol higher energy bar-  
533 rier than the first hydrogen transfer on the kite-like  $\text{Fe}_2\text{O}_3$  cluster.  
534 This reaction also involves different isomers of  $(\text{Fe}_2\text{O}_3)_2$ , where  
535 decomposition takes place on the second minima isomer of  $(\text{Fe}_2\text{O}_3)_2$   
536 shown in Fig. S3. The relative binding energy of the second minima  
537 isomer is 2.35 kcal/mol. The second dehydrogenation step that fol-  
538 lows from the adsorbate  $\text{NH}_2^*$  intermediate ( $\text{I}_22$ ) further dissociates  
539 to  $\text{NH}^* + 2\text{H}^*$ , in which the dissociated hydrogen atom is subse-  
540 quently transferred to another neighboring oxygen as shown in the  
541 reaction path ( $\text{I}_22$ – $\text{T}_22$ – $\text{I}_23$ ). This reaction occurs with an energy  
542 barrier of 38.57 kcal/mol. The ultimate dehydrogenation step is the  
543 formation of  $\text{N}^* + 3\text{H}^*$ , where N is bound to the central top  $\text{Fe}^{3+}$   
544 and all the hydrogen atoms interact with three neighboring oxygens.  
545 The last dehydrogenation step occurs with an energy barrier of 3.86  
546 kcal/mol higher than the energy barrier of the second dehydrogena-  
547 tion step, and it is shown in the reaction pathway ( $\text{I}_23$ – $\text{T}_23$ – $\text{I}_24$ ).  
548 It suggests that the dehydrogenation of adsorbate  $\text{NH}^*$  is a rate-  
549 determining step on the  $(\text{Fe}_2\text{O}_3)_2$  cluster. Moreover, from a ther-  
550 modynamic viewpoint, the calculated dehydrogenation steps of

$\text{NH}_3$  on the  $(\text{Fe}_2\text{O}_3)_2$  cluster are endothermic by 8.12, 18.6, and  
23.78 kcal/mol.

We consider the  $\text{H}_2$  formation reactions via two reaction path-  
ways. The first  $\text{H}_2$  formation reaction (11) occurs with the partial  
decomposition of  $\text{NH}_3$  starting from intermediates ( $\text{I}_23$ ) through  
( $\text{I}_29$ ). In the first stage through this reaction path starting from ( $\text{I}_23$ ),  
the transition state ( $\text{T}_26$ ) was found, where the H atom adsorbed  
onto the Fe atom, forming an Fe–H bond. In the second stage of  
the reaction, the transition state ( $\text{T}_27$ ) was the one that splits the  
adsorbed H atom from the adjacent O atom to form adsorbed  $\text{NH}^*$ .  
Then, the dissociated H atom was adsorbed onto the O atom, which  
is an adjacent atom to the Fe–H bond, and at the final stage, the  
dissociative molecular  $\text{H}_2$  formed via ( $\text{T}_28$ ), and the barrier of this  
reaction is 91.1 kcal/mol.

The complete reaction pathway for reaction (11) is  
( $\text{I}_23$ – $\text{T}_26$ – $\text{I}_27$ – $\text{T}_27$ – $\text{I}_28$ – $\text{T}_28$ – $\text{I}_29$ ). The second  $\text{H}_2$  formation  
reaction (12) occurs with the fully decomposed  $\text{NH}_3$  molecule  
starting from the intermediate ( $\text{I}_24$ ) through the intermediate ( $\text{I}_26$ ).  
It is important to note that the last dehydrogenation reaction (10)  
is the one that has the highest barrier on the  $(\text{Fe}_2\text{O}_3)_2$  cluster.  
So, the dissociative molecular hydrogen formation through this  
reaction path costs an energy as shown in the reaction path  
( $\text{I}_24$ – $\text{T}_24$ – $\text{I}_25$ – $\text{T}_25$ – $\text{I}_26$ ). Overall, as it seen from the depicted  
reaction pathways in Fig. 8, the  $\text{H}_2$  formation reaction is kinetically  
and energetically costly in the reaction  $\text{N}^* + 3\text{H}^* \rightarrow \text{N}^* + \text{H}^* + \text{H}_2$ ,  
and it is more favorable via the reaction  $\text{NH}^* + 2\text{H}^* \rightarrow \text{NH}^* + \text{H}_2$ ,  
which is the partial decomposition of  $\text{NH}_3$  on the  $(\text{Fe}_2\text{O}_3)_2$  cluster.

551  
552  
553  
554  
555  
556  
557  
558  
559  
560  
561  
562  
563  
564  
565  
566  
567  
568  
569  
570  
571  
572  
573  
574  
575  
576  
577

### E. NH<sub>3</sub> decomposition on Fe<sub>6</sub>O<sub>9</sub>

The energy profile for the stepwise dehydrogenation of NH<sub>3</sub> on the (Fe<sub>2</sub>O<sub>3</sub>)<sub>3</sub> cluster is presented in Fig. 9(a), while the intermediate and transition state structures along this reaction pathway are shown in Fig. 9(b). The dissociation of NH<sub>3</sub> on the (Fe<sub>2</sub>O<sub>3</sub>)<sub>3</sub> cluster is more complex compared to smaller Fe(III) oxide structures, as NH<sub>3</sub> can adsorb at various sites on the (Fe<sub>2</sub>O<sub>3</sub>)<sub>3</sub> surface.

We identified the most favorable adsorption configuration, I<sub>3</sub>1, with an adsorption energy of  $\Delta G = -18.8$  kcal/mol, from which the stepwise decomposition reaction proceeds. The first dehydrogenation reaction, as described in (8), begins with NH<sub>3</sub><sup>\*</sup> adsorbed on the (Fe<sub>2</sub>O<sub>3</sub>)<sub>3</sub> cluster as I<sub>3</sub>1 and proceeds through the transition state T<sub>3</sub>1. The energy barrier along this pathway is 20.04 kcal/mol, which is lower than the barrier for the first H abstraction from NH<sub>3</sub> on the (Fe<sub>2</sub>O<sub>3</sub>)<sub>2</sub> cluster. Although the first dehydrogenation reaction on the (Fe<sub>2</sub>O<sub>3</sub>)<sub>3</sub> cluster is endothermic, we observed that when the NH<sub>2</sub><sup>\*</sup> species migrates to a bridging position between two Fe atoms (Fe–N–Fe), the reaction becomes exothermic by 14.15 kcal/mol, as shown in the reaction pathways I<sub>3</sub>2–T<sub>3</sub>2–I<sub>3</sub>3 and I<sub>3</sub>3–T<sub>3</sub>3–I<sub>3</sub>4.

The second H abstraction involves a further dehydrogenation of NH<sub>2</sub><sup>\*</sup> into NH<sup>\*</sup> and H<sup>\*</sup>, with an energy barrier of 35.97 kcal/mol along the pathway I<sub>3</sub>4–T<sub>3</sub>4–I<sub>3</sub>5. This barrier is 15.96 kcal/mol higher than that of the first dehydrogenation step. In addition, this reaction is endothermic, with a reaction energy of 15.74 kcal/mol.

Similarly, in the third step (10), the remaining NH<sup>\*</sup> dissociates into N<sup>\*</sup> and H<sup>\*</sup>, with an energy barrier of 17.94 kcal/mol higher than that of the second dissociation step. This is the largest barrier encountered in the decomposition of NH<sub>3</sub>. The calculated reaction

pathway indicates that this process is endothermic, with a reaction energy of 25.76 kcal/mol.

Finally, the possible H<sub>2</sub> formation reactions [(11) and (12)] on the (Fe<sub>2</sub>O<sub>3</sub>)<sub>3</sub> cluster were calculated, as shown in Fig. 9. The first H<sub>2</sub> formation reaction (11) begins with one adsorbed NH<sup>\*</sup> and two H<sup>\*</sup> species on the (Fe<sub>2</sub>O<sub>3</sub>)<sub>3</sub> cluster. The reaction proceeds in a manner similar to that discussed in Subsection III D: the adsorbed H<sup>\*</sup> on oxygen, adjacent to NH<sup>\*</sup> adsorbed on Fe, migrates away by forming Fe–H bonds through the transition states T<sub>3</sub>7 and T<sub>3</sub>8. The overall energy barrier for H<sub>2</sub> formation via reaction (11) is 100.74 kcal/mol.

The second possible H<sub>2</sub> formation pathway starts from fully decomposed NH<sub>3</sub> (I<sub>3</sub>6) and proceeds through the transition state T<sub>3</sub>6. This pathway has a significantly high energy barrier, calculated to be 116.89 kcal/mol, as shown in the reaction path I<sub>3</sub>6–T<sub>3</sub>6–I<sub>3</sub>7. These results suggest that, from both a thermodynamic and a kinetic perspective, H<sub>2</sub> formation after full dehydrogenation of NH<sub>3</sub> is less favorable.

### F. NH<sub>3</sub> decomposition on Fe<sub>8</sub>O<sub>12</sub>

Finally, the decomposition of NH<sub>3</sub> and the H<sub>2</sub> formation pathways on the (Fe<sub>2</sub>O<sub>3</sub>)<sub>4</sub> cluster is illustrated in Fig. 10(a), with the intermediate and transition state structures shown in Fig. 10(b). As discussed in Secs. III A–III E, increasing the number of units *n* in (Fe<sub>2</sub>O<sub>3</sub>)<sub>*n*</sub> increases the number of active sites that interact with NH<sub>3</sub>. However, similar to the reactions on (Fe<sub>2</sub>O<sub>3</sub>)<sub>*n*</sub> (*n* = 2, 3), the most stable adsorption site for NH<sub>3</sub> on (Fe<sub>2</sub>O<sub>3</sub>)<sub>4</sub> is a three-coordinated Fe site, with an adsorption energy of  $-19.2$  kcal/mol

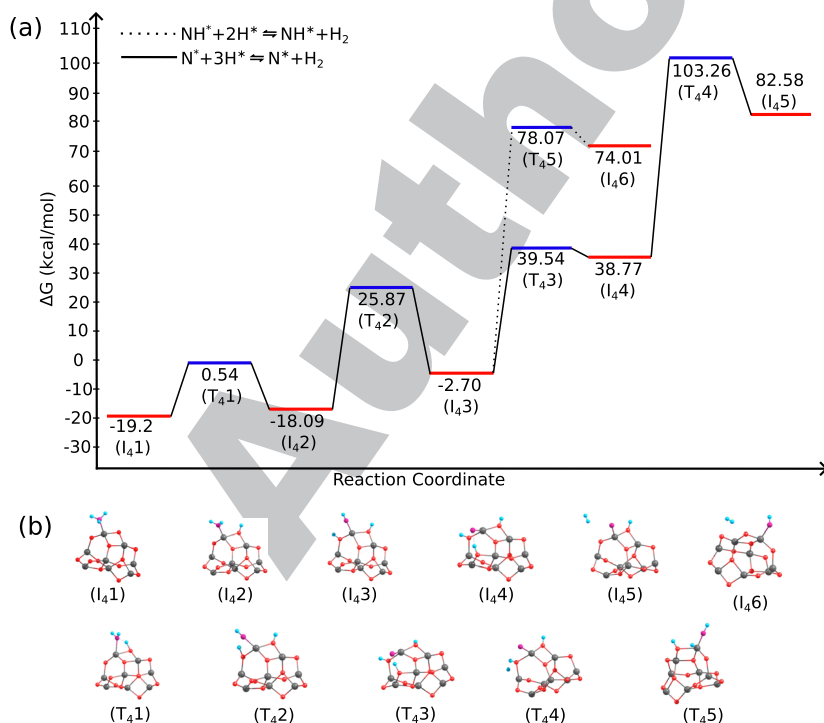


FIG. 10. (a) Energy profile for the NH<sub>3</sub><sup>\*</sup> → NH<sub>2</sub><sup>\*</sup> + H<sup>\*</sup> → NH<sup>\*</sup> + 2H<sup>\*</sup> → N<sup>\*</sup> + 3H<sup>\*</sup> and H<sub>2</sub> formation reaction paths on the (Fe<sub>2</sub>O<sub>3</sub>)<sub>4</sub> cluster at T = 298.15 K. (b) Geometries of the optimized equilibrium and transition states along the reaction path.

at room temperature, slightly higher than that on  $(\text{Fe}_2\text{O}_3)_3$ . The dehydrogenation of  $\text{NH}_3$  begins with the adsorption of  $\text{NH}_3^*$ , as shown in the intermediate state  $\text{I}_41$ . The first dehydrogenation step involves breaking one N–H bond and forming an O–H bond, with an energy barrier of 19.74 kcal/mol, as shown in the reaction pathway  $\text{I}_41\text{--T}_41\text{--I}_42$ . The second dehydrogenation step (9) involves the dissociation of  $\text{NH}_2^* + \text{H}^*$  to form  $\text{NH}^* + 2\text{H}^*$ , proceeding through the transition state  $\text{T}_42$ . The energy barrier for this step is 43.96 kcal/mol, which is higher than the corresponding second dehydrogenation steps on  $(\text{Fe}_2\text{O}_3)_n$  ( $n = 1\text{--}3$ ). The final dehydrogenation step occurs along the pathway  $\text{I}_43\text{--T}_43\text{--I}_44$ , with a barrier of 42.24 kcal/mol. All  $\text{NH}_3$  dehydrogenation steps on  $(\text{Fe}_2\text{O}_3)_4$  are endothermic, with reaction energies of 1.11, 15.39, and 41.47 kcal/mol, respectively.

The final reaction pathway on the  $(\text{Fe}_2\text{O}_3)_4$  cluster involves  $\text{H}_2$  formation from both partially and fully decomposed  $\text{NH}_3$ , as described in (11) and (12). As observed for all sizes of  $(\text{Fe}_2\text{O}_3)_n$  clusters,  $\text{H}_2$  formation is energetically more favorable after the partial decomposition of  $\text{NH}_3$  in reaction (11) compared to the fully decomposed pathway (12). However, this pathway also presents the highest energy barrier on this cluster.

#### IV. COMPARISON AND CONCLUSION

Our results, illustrated in Figs. 4, 5, and 8–10, indicate that  $\text{NH}_3$  dehydrogenation can be a thermodynamically favorable reaction on  $(\text{Fe}_2\text{O}_3)_n$  ( $n = 1\text{--}4$ ) clusters. However, the favorability depends on the size and geometry of the cluster, as well as the specific reaction steps described in (8)–(12).

To compare the activity of various sizes and structures of  $(\text{Fe}_2\text{O}_3)_n$  ( $n = 1\text{--}4$ ), we have calculated the change in Gibbs free energy ( $\Delta G$ ) as a function of temperature at 1 bar pressure, as shown in Fig. S6. Across all reactions studied, we observed that  $\Delta G$  increases with temperature. This suggests that  $\text{NH}_3$  dehydrogenation on  $(\text{Fe}_2\text{O}_3)_n$  ( $n = 2, 4$ ) can be energetically favorable at moderate temperatures, depending on the specific reaction step. However, as the temperature rises beyond a certain threshold, the reaction becomes unfavorable.

For example, as shown in Figs. S6(a)–S6(c), all dehydrogenation reactions on  $(\text{Fe}_2\text{O}_3)_n$  ( $n = 1$ ) are energetically favorable within the temperature range of 0–1000 K. In contrast, on  $(\text{Fe}_2\text{O}_3)_n$  ( $n = 2, 4$ ), only the last dehydrogenation step is limiting. Since  $\Delta G$  of the third dehydrogenation reaction is already greater than zero at 0 K, this step is not favorable at any temperature. Another larger cluster considered in this study,  $(\text{Fe}_2\text{O}_3)_n$  ( $n = 3$ ), exhibits better stability of the reaction intermediates during the second dehydrogenation step, remaining favorable up to 800 K. Meanwhile, the second dehydrogenation reaction on  $(\text{Fe}_2\text{O}_3)_n$  ( $n = 4$ ) is favorable only up to 400 K. The most endothermic dehydrogenation reaction on this cluster is the step  $\text{NH}^* + 2\text{H}^* \rightarrow \text{N}^* + 3\text{H}^*$ . The first and second dehydrogenation steps are favorable up to 1100 and 700 K, respectively. Moreover, we observed the variation in  $\Delta G$  with temperature for the  $\text{H}_2$  formation reaction on  $(\text{Fe}_2\text{O}_3)_n$  ( $n = 1\text{--}4$ ). Our results indicate that the formation of molecular hydrogen is not thermodynamically favorable at any temperature. However, temperature is not the only factor determining whether the reaction occurs. If sufficient energy is available to overcome the activation barrier, the reaction can still proceed.

The effective production of molecular hydrogen from ammonia is determined by the stepwise dehydrogenation of adsorbed ammonia on the catalyst. Catalytic reaction mechanisms are analyzed by identifying the rate-determining step in the dehydrogenation of  $\text{NH}_3$ , which corresponds to the step requiring the highest energy to activate the N–H bond. However, it is important to note that in catalysis, the overall energy barrier is more significant than the barrier for any single intermediate reaction step.

Several studies have reported different rate-determining steps depending on the type of catalyst used.<sup>64</sup> Lu *et al.* found that the rate-determining step in  $\text{NH}_3$  decomposition on different phases of Ru surface catalysts is the formation of molecular nitrogen.<sup>65</sup> In contrast, studies by Zhang *et al.*<sup>19</sup> on ammonia decomposition on small iron clusters showed that the rate-determining step on single Fe and  $\text{Fe}_3$  is the  $\text{NH}^* \rightarrow \text{N}^* + \text{H}^*$  step, whereas for  $\text{Fe}_2$  and  $\text{Fe}_4$ , the rate-determining step is the  $\text{NH}_2^* \rightarrow \text{NH}^* + \text{H}^*$  step. Similarly, a detailed comparison of the energy barriers for each elementary step in  $\text{NH}_3$  decomposition and  $\text{H}_2$  formation on different sizes and shapes of  $(\text{Fe}_2\text{O}_3)_n$  ( $n = 1\text{--}4$ ) is shown in Fig. 11. Based on the results from our calculations, the rate-determining step in ammonia decomposition and  $\text{H}_2$  formation varies with the size of the  $(\text{Fe}_2\text{O}_3)_n$  ( $n = 1\text{--}4$ ) oxide clusters. In general, the final step of  $\text{H}_2$  formation represents the highest energy barrier on all  $(\text{Fe}_2\text{O}_3)_n$  ( $n = 1\text{--}4$ ) clusters. However, the analysis of  $\text{NH}_3$  decomposition shows that the  $\text{NH}^* \rightarrow \text{N}^* + \text{H}^*$  step is typically the rate-determining step, except in the case of  $(\text{Fe}_2\text{O}_3)_4$ , where the rate-determining step is the second H dissociation step. Furthermore, the first dehydrogenation step exhibits an energy barrier that is nearly identical across all clusters, with the process being exothermic for clusters  $n = 1$  and  $n = 3$  and endothermic for clusters  $n = 2$  and  $n = 4$ . For the second dehydrogenation step,  $(\text{Fe}_2\text{O}_3)_3$  demonstrates a significantly higher activity compared to the other cluster sizes. It is also important to note that  $n = 1$  (linear) is the only special configuration of  $\text{Fe}_2\text{O}_3$  containing two terminal  $\text{O}^{2-}$  ions, unlike the other types of  $\text{Fe}_2\text{O}_3$ , which may promote a potentially high activity for  $\text{NH}_3$  dehydrogenation and molecular hydrogen formation. Overall, the lowest energy barrier observed for  $\text{H}_2$  formation is associated with the largest cluster considered in this study.

In this research, various structures of  $(\text{Fe}_2\text{O}_3)_n$  ( $n = 1\text{--}4$ ) were obtained using the SC-AFIR method, and we investigated the ammonia decomposition and molecular hydrogen formation reaction pathways on the most stable isomers of  $(\text{Fe}_2\text{O}_3)_n$  ( $n = 1\text{--}4$ ) clusters. This analysis employed the SC-AFIR and DS-AFIR methods within the Global Reaction Route Mapping (GRRM) strategy, utilizing the B3LYP exchange–correlation functional in Kohn–Sham DFT.

The results indicate that the catalytic activity in ammonia decomposition varies depending on the size and shape of the high-spin iron trioxides. The adsorption analysis reveals that the  $\text{NH}_3$  molecule preferentially adsorbs at two-coordinated Fe sites in  $n = 1$  and at three-coordinated Fe sites in  $n = 2\text{--}4$  clusters. Furthermore, the adsorption energy tends to decrease from  $n = 1$  to  $n = 3$  of the  $(\text{Fe}_2\text{O}_3)_n$  clusters and then slightly increases for the  $(\text{Fe}_2\text{O}_3)_4$  cluster. From a thermodynamic perspective, the adsorption of the  $\text{NH}_3$  molecule on  $\text{Fe}_2\text{O}_3$  is favorable across the whole range of the considered temperatures from 0 to 1200 K. In contrast, for the larger clusters  $(\text{Fe}_2\text{O}_3)_n$  ( $n = 2, 4$ ), ammonia adsorption becomes energetically unfavorable at temperatures of 1140, 940, and 989 K for  $n = 2, 3,$



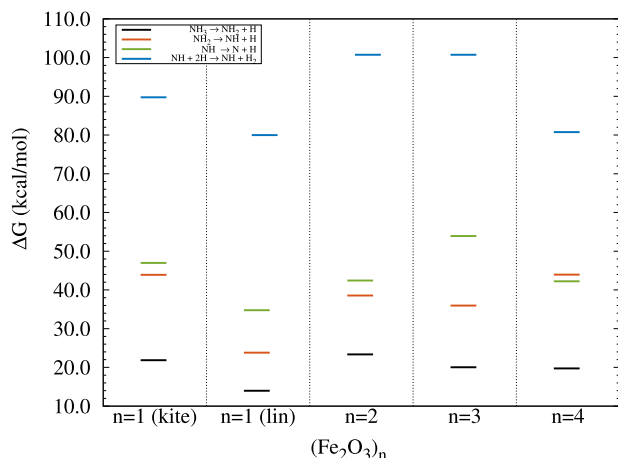


FIG. 11. Reaction barrier ( $\Delta G^\ddagger$ ) for  $\text{NH}_3$  dehydrogenation and  $\text{H}_2$  formation reactions on  $(\text{Fe}_2\text{O}_3)_n$  ( $n = 1-4$ ) clusters.

and 4, respectively. A comparison of the rate-determining steps in the ammonia dehydrogenation reaction reveals a dependency on the size of the iron trioxide clusters. Thus, the reaction step  $\text{NH}^* \rightarrow \text{N}^* + \text{H}^*$  is the rate-determining step for the smaller iron trioxide clusters  $(\text{Fe}_2\text{O}_3)_n$  ( $n = 1-3$ ). In contrast, the reaction step  $\text{NH}_2^* \rightarrow \text{NH}^* + \text{H}^*$  is identified as the rate-determining step for the  $(\text{Fe}_2\text{O}_3)_n$  ( $n = 4$ ) cluster. In addition, we observed that the energy barrier for molecular hydrogen formation increases with the size of the clusters  $(\text{Fe}_2\text{O}_3)_n$  ( $n = 1-3$ ) but then experiences a drastic decrease for the  $(\text{Fe}_2\text{O}_3)_4$  cluster.

We have investigated the catalytic activity of high-spin  $(\text{Fe}_2\text{O}_3)_n$  ( $n = 1-4$ ) clusters for the decomposition of  $\text{NH}_3$ . We believe that the results are valuable for designing iron trioxide-based nanosized catalysts by regulating the size of the  $(\text{Fe}_2\text{O}_3)_n$  clusters to enhance  $\text{H}_2$  production from the catalytic decomposition of ammonia.

## SUPPLEMENTARY MATERIAL

The supplementary material provides the energies and structures of the lowest-energy isomers of  $(\text{Fe}_2\text{O}_3)_n$  ( $n = 1-4$ ) clusters and the change in Gibbs free energy with temperature for each dehydrogenation step.

## ACKNOWLEDGMENTS

This work was partly supported by the MEXT Program: Data Creation and Utilization-Type Material Research and Development Project Grant No. JPMXP1122712807 and partially supported by NAWA "STE(E)R-ING towards International Doctoral School." Calculations were performed using the computational resources of the Institute for Solid State Physics, the University of Tokyo, Japan, and the Research Center for Computational Science, Okazaki, Japan (Project No. 23-IMS-C016). S.I. acknowledges the MANABIYA system of the Institute for Chemical Reaction Design and Discovery

(ICReDD) of Hokkaido University, which was established by the World Premier International Research Initiative (WPI), MEXT, Japan, to support the learning of the GRRM program techniques for DFT calculations.

## AUTHOR DECLARATIONS

### Conflict of Interest

The authors have no conflicts to disclose.

## Author Contributions

**Sapajan Ibragimov:** Data curation (equal); Investigation (equal); Writing – original draft (equal); Writing – review & editing (equal). **Andrey Lyalin:** Conceptualization (equal); Supervision (equal); Writing – review & editing (equal). **Sonu Kumar:** Investigation (equal); Writing – review & editing (equal). **Yuriko Ono:** Methodology (equal); Writing – review & editing (equal). **Tetsuya Taketsugu:** Supervision (equal); Writing – review & editing (equal). **Maciej Bobrowski:** Supervision (equal); Writing – review & editing (equal).

## DATA AVAILABILITY

The data that support the findings of this study are available from the corresponding author upon reasonable request.

## REFERENCES

- D. A. Hansgen, D. G. Vlachos, and J. G. Chen, *Nat. Chem.* **2**, 484 (2010).
- C. Plana, S. Armenise, A. Monzón, and E. García-Bordejé, *J. Catal.* **275**, 228 (2010).
- H. Liu, H. Wang, J. Shen, Y. Sun, and Z. Liu, *Catal. Today* **131**, 444 (2008).
- R. Lan, J. T. Irvine, and S. Tao, *Int. J. Hydrogen Energy* **37**, 1482 (2012).
- A. Klerke, C. H. Christensen, J. K. Nørskov, and T. Vegge, *J. Mater. Chem.* **18**, 2304 (2008).
- J. C. Ganley, F. Thomas, E. Seebauer, and R. I. Masel, *Catal. Lett.* **96**, 117 (2004).
- S.-F. Yin, Q.-H. Zhang, B.-Q. Xu, W.-X. Zhu, C.-F. Ng, and C.-T. Au, *J. Catal.* **224**, 384 (2004).
- Á. Logadóttir and J. K. Nørskov, *J. Catal.* **220**, 273 (2003).
- I. Lucentini, X. Garcia, X. Vendrell, and J. Llorca, *Ind. Eng. Chem. Res.* **60**, 18560 (2021).
- L. Yao, T. Shi, Y. Li, J. Zhao, W. Ji, and C.-T. Au, *Catal. Today* **164**, 112 (2011).
- K. Zemski, D. Justes, and A. Castleman, *J. Phys. Chem. B* **106**, 6136 (2002).
- D. Yang, M. Babucci, W. H. Casey, and B. C. Gates, *ACS Cent. Sci.* **6**, 1523 (2020).
- E. C. Tyo and S. Vajda, *Nat. Nanotechnol.* **10**, 577 (2015).
- U. Heiz and U. Landman, *Nanocatalysis* (Springer Science & Business Media, 2007).
- A. Fernando, K. L. D. M. Weerawardene, N. V. Karimova, and C. M. Aikens, *Chem. Rev.* **115**, 6112 (2015).
- K. Nishimaki, S. Ohmae, T. Yamamoto, and M. Katsura, *Nanostruct. Mater.* **12**, 527 (1999).
- G. Lanzani and K. Laasonen, *Int. J. Hydrogen Energy* **35**, 6571 (2010).
- G. S. Otero, B. Pascucci, M. M. Branda, R. Miotto, and P. G. Belelli, *Comput. Mater. Sci.* **124**, 220 (2016).
- X. Zhang, Z. Lu, D. Ma, and Z. Yang, *Int. J. Hydrogen Energy* **40**, 346 (2015).
- J. Zhang, H. Xu, X. Jin, Q. Ge, and W. Li, *Appl. Catal., A* **290**, 87 (2005).

- 831 <sup>21</sup>A. M. Karim, V. Prasad, G. Mpourmpakis, W. W. Lonergan, A. I. Frenkel, J. G.  
832 Chen, and D. G. Vlachos, *J. Am. Chem. Soc.* **131**, 12230 (2009).
- 833 <sup>22</sup>J. Ji, X. Duan, G. Qian, P. Li, X. Zhou, D. Chen, and W. Yuan, *Catal. Today* **216**,  
254 (2013).
- 834 <sup>23</sup>J. Zhang, M. Comotti, F. Schüth, R. Schlögl, and D. S. Su, *Chem. Commun.*  
835 **2007**, 1916.
- 836 <sup>24</sup>X. Duan, J. Zhou, G. Qian, P. Li, X. Zhou, and D. Chen, *Chin. J. Catal.* **31**, 979  
(2010).
- 837 <sup>25</sup>Q. Yang, X.-P. Fu, C.-J. Jia, C. Ma, X. Wang, J. Zeng, R. Si, Y.-W. Zhang, and  
838 C.-H. Yan, *ACS Catal.* **6**, 3072 (2016).
- Q10 839 <sup>26</sup>N. Iordanova, M. Dupuis, and K. M. Rosso, *J. Chem. Phys.* **122**, 144305 (2005).
- 840 <sup>27</sup>M. Sánchez, L. Sabio, N. Gálvez, M. Capdevila, and J. M. Dominguez-Vera,  
841 *IUBMB Life* **69**, 382 (2017).
- 842 <sup>28</sup>L. Machala, J. Tucek, and R. Zboril, *Chem. Mater.* **23**, 3255 (2011).
- Q11 843 <sup>29</sup>F. Yingying, W. Jie, and D. Yong, ■ ■ ■ (2016).
- 844 <sup>30</sup>Q. Shi, Y. Zhou, J. Cheng, Y. Pan, Y. Wu, L. Zhu, and Z. Yuan, *Microporous*  
845 *Mesoporous Mater.* **332**, 111681 (2022).
- 846 <sup>31</sup>H. Zhao, M. Jiang, Q. Kang, L. Liu, N. Zhang, P. Wang, and F. Zhou, *Catal. Sci.*  
847 *Technol.* **10**, 8305 (2020).
- 848 <sup>32</sup>S. Maeda, T. Taketsugu, and K. Morokuma, *J. Comput. Chem.* **35**, 166 (2014).
- 849 <sup>33</sup>W. Sameera, A. Kumar Sharma, S. Maeda, and K. Morokuma, *Chem. Rec.* **16**,  
850 2349 (2016).
- 851 <sup>34</sup>A. D. Becke, *J. Chem. Phys.* **98**, 5648 (1993).
- 852 <sup>35</sup>P. J. Stephens, F. J. Devlin, C. F. Chabalowski, and M. J. Frisch, *J. Phys. Chem.*  
853 **98**, 11623 (1994).
- 854 <sup>36</sup>R. H. Hertwig and W. Koch, *Chem. Phys. Lett.* **268**, 345 (1997).
- 855 <sup>37</sup>P. J. Hay and W. R. Wadt, *J. Chem. Phys.* **82**, 270 (1985).
- 856 <sup>38</sup>W. R. Wadt and P. J. Hay, *J. Chem. Phys.* **82**, 284 (1985).
- 857 <sup>39</sup>P. J. Hay and W. R. Wadt, *J. Chem. Phys.* **82**, 299 (1985).
- 858 <sup>40</sup>M. J. Frisch, G. W. Trucks, H. B. Schlegel, G. E. Scuseria, M. A. Robb, J. R.  
859 Cheeseman, G. Scalmani, V. Barone, G. A. Petersson, H. Nakatsuji, X. Li, M. Car-  
860 icato, A. V. Marenich, J. Bloino, B. G. Janesko, R. Gomperts, B. Mennucci, H.  
861 P. Hratchian, J. V. Ortiz, A. F. Izmaylov, J. L. Sonnenberg, D. Williams-Young,  
862 F. Ding, F. Lipparini, F. Egidi, J. Goings, B. Peng, A. Petrone, T. Henderson, D.  
863 Ranasinghe, V. G. Zakrzewski, J. Gao, N. Rega, G. Zheng, W. Liang, M. Hada,  
864 M. Ehara, K. Toyota, R. Fukuda, J. Hasegawa, M. Ishida, T. Nakajima, Y. Honda,  
865 O. Kitao, H. Nakai, T. Vreven, K. Throssell, J. A. Montgomery, Jr., J. E. Peralta, F.  
866 Ogliaro, M. J. Bearpark, J. J. Heyd, E. N. Brothers, K. N. Kudin, V. N. Staroverov, T.  
867 A. Keith, R. Kobayashi, J. Normand, K. Raghavachari, A. P. Rendell, J. C. Burant,  
868 S. S. Iyengar, J. Tomasi, M. Cossi, J. M. Millam, M. Klene, C. Adamo, R. Cammi,  
869 J. W. Ochterski, R. L. Martin, K. Morokuma, O. Farkas, J. B. Foresman, and D. J.  
870 Fox, Gaussian 16, Revision C.01, Gaussian, Inc., Wallingford, CT, 2016.
- 871 <sup>41</sup>M. N. Glukhovtsev, R. D. Bach, and C. J. Nagel, *J. Phys. Chem. A* **101**, 316  
(1997).
- 872 <sup>42</sup>T. Taguchi, T. C. Stamatatos, K. A. Abboud, C. M. Jones, K. M. Poole, T. A.  
873 O'Brien, and G. Christou, *Inorg. Chem.* **47**, 4095 (2008).
- 874 <sup>43</sup>S. Maeda and K. Morokuma, *J. Chem. Phys.* **132**, 241102 (2010).
- 875 <sup>44</sup>S. Maeda and K. Morokuma, *J. Chem. Theory Comput.* **7**, 2335 (2011).
- 876 <sup>45</sup>S. Maeda, K. Ohno, and K. Morokuma, *Phys. Chem. Chem. Phys.* **15**, 3683  
(2013).
- 877 <sup>46</sup>S. Maeda, Y. Harabuchi, M. Takagi, K. Saita, K. Suzuki, T. Ichino, Y. Sumiya, K.  
878 Sugiyama, and Y. Ono, "Implementation and performance of the artificial force  
879 induced reaction method in the GRRM17 program," *J. Comput. Chem.* **39**, 233  
(2018).
- 880 <sup>47</sup>A. K. Sharma, W. Sameera, M. Jin, L. Adak, C. Okuzono, T. Iwamoto, M. Kato,  
881 M. Nakamura, and K. Morokuma, *J. Am. Chem. Soc.* **139**, 16117 (2017).
- 882 <sup>48</sup>B. B. Skjelstad, T. Helgaker, S. Maeda, and D. Balcells, *ACS Catal.* **12**, 12326  
(2022).
- 883 <sup>49</sup>M. Gao, A. Lyalin, S. Maeda, and T. Taketsugu, *J. Chem. Theory Comput.* **10**,  
884 1623 (2014).
- 885 <sup>50</sup>M. Gao, A. Lyalin, M. Takagi, S. Maeda, and T. Taketsugu, *J. Phys. Chem. C*  
886 **119**, 11120 (2015).
- 887 <sup>51</sup>A. Hellman, K. Honkala, I. Remediakis, A. Logadottir, A. Carlsson, S. Dahl, C.  
888 H. Christensen, and J. K. Nørskov, *Surf. Sci.* **603**, 1731 (2009).
- 889 <sup>52</sup>H. Shiroishi, T. Oda, I. Hamada, and N. Fujima, *Eur. Phys. J. D* **24**, 85 (2003).
- 890 <sup>53</sup>N. Jones, B. Reddy, F. Rasouli, and S. N. Khanna, *Phys. Rev. B* **72**, 165411 (2005).
- 891 <sup>54</sup>A. Erlebach, C. Hühn, R. Jana, and M. Sierka, *Phys. Chem. Chem. Phys.* **16**,  
892 26421 (2014).
- 893 <sup>55</sup>Y. Zhao and D. G. Truhlar, *Theor. Chem. Acc.* **120**, 215 (2008).
- 894 <sup>56</sup>N. Mardirossian and M. Head-Gordon, *Phys. Chem. Chem. Phys.* **16**, 9904  
(2014).
- 895 <sup>57</sup>S. Zhou, S. Lin, and H. Guo, *J. Phys. Chem. C* **122**, 9091 (2018).
- 896 <sup>58</sup>C. Zhang, M. Lynch, and P. Hu, *Surf. Sci.* **496**, 221 (2002).
- 897 <sup>59</sup>W. Huang, L. Wang, L. Dong, H. Hu, and D. Ren, *Molecules* **28**, 2371 (2023).
- 898 <sup>60</sup>C.-y. Zou, W. Ji, Z. Shen, Q. Tang, and M. Fan, *Appl. Surf. Sci.* **442**, 778  
(2018).
- 899 <sup>61</sup>C. Xie, Y. Sun, B. Zhu, W. Song, and M. Xu, *New J. Chem.* **45**, 3169 (2021).
- 900 <sup>62</sup>D. Ren and K. Gui, *Appl. Surf. Sci.* **487**, 171 (2019).
- 901 <sup>63</sup>E. Erdtman, M. Andersson, A. L. Spetz, and L. Ojamäe, *Surf. Sci.* **656**, 77 (2017).
- 902 <sup>64</sup>S. R. Kulkarni, N. Realpe, A. Yerrayya, V. K. Velisoju, S. Sayas, N. Morlanes, J.  
903 Cerillo, S. P. Katikaneni, S. N. Paglieri, B. Solami *et al.*, *Catal. Sci. Technol.* **13**,  
904 2026 (2023).
- 905 <sup>65</sup>X. Lu, J. Zhang, W.-K. Chen, and A. Roldan, *Nanoscale Adv.* **3**, 1624 (2021).